ACS APPLIED ELECTRONIC MATERIALS

pubs.acs.org/acsaelm

Article

Fine-Tuning the Performance of Ultraflexible Organic Complementary Circuits on a Single Substrate via a Nanoscale Interfacial Photochemical Reaction

Koki Taguchi, Takafumi Uemura,* Andreas Petritz, Naoko Namba, Mihoko Akiyama, Masahiro Sugiyama, Teppei Araki, Barbara Stadlober, and Tsuyoshi Sekitani*

Cite This: *ACS Appl. Electron. Mater.* 2022, 4, 6308−6321

Read Online

ACCESS | Metrics & More | Article Recommendations | Supporting Information

ABSTRACT: Flexible electronics has paved the way toward the development of next-generation wearable and implantable healthcare devices, including multimodal sensors. Integrating flexible circuits with transducers on a single substrate is desirable for processing vital signals. However, the trade-off between low power consumption and high operating speed is a major bottleneck. Organic thin-film transistors (OTFTs) are suitable for developing flexible circuits owing to their intrinsic flexibility and compatibility with the printing process. We used a photoreactive insulating polymer poly((±)endo,exo-bicyclo[2.2.1]hept-ene-2,3-dicarboxylic acid, diphenylester) (PNDPE) to modulate the power consumption and operating speed of ultraflexible organic circuits fabricated on a single substrate. The turn-on voltage (V_{on}) of the p- and n-type OTFTs was controlled through a nanoscale interfacial photochemical reaction. The time-of-flight secondary ion mass spectrometry revealed the preferential occurrence of the PNDPE photochemical reaction in the vicinity of the semiconductor−dielectric interface. The power consumption and operating speed of the ultraflexible complementary inverters were tuned by a factor of 6 and 4, respectively. The minimum static power consumption was 30 ± 9 pW at transient and 4 ± 1 pW at standby. Furthermore, within the tuning range of the operating speed and at a supply voltage above 2.5 V, the minimum stage delay time was of the order of hundreds of microseconds. We demonstrated electromyogram measurements to emphasize the advantage of the nanoscale interfacial photochemical reaction. Our study suggests that a nanoscale interfacial photochemical reaction can be employed to develop imperceptible and wearable multimodal sensors with organic signal processing circuits that exhibit low power consumption.

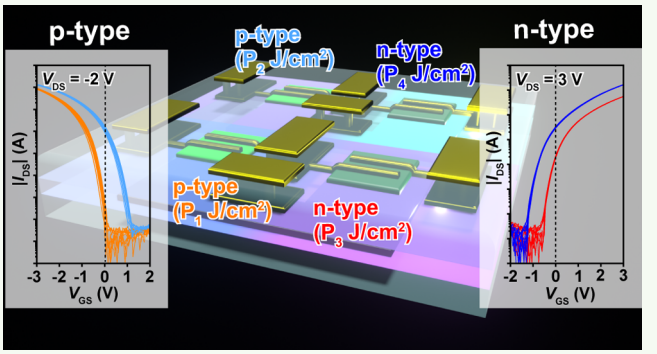

KEYWORDS: *flexible electronics, organic thin-film transistors, polymer gate dielectrics, organic complementary circuits, turn-on voltage, threshold voltage control, biosignal measurement*

INTRODUCTION

Flexible electronics is a promising technology for developing next-generation wearable and implantable healthcare devices that can be used for imperceptible and long-term biosignal monitoring as well as in medical surgery.[1−9] One such recently developed flexible healthcare device is a multimodal sensor.[10−15] The multimodal sensor provides highly accurate results, which aid in obtaining a deep understanding of human health. Moreover, chemical and physical monitoring are crucial for obtaining information on glucose levels, pH levels, lactate production, and heart conditions (via electrocardiograms).[10−13]

Integrating flexible circuits with transducers is necessary for processing vital signals while retaining the imperceptibility of multimodal sensors. The trade-off between low power consumption and high operating speed of circuits is a major challenge, especially when the multimodal sensor is fabricated on a single substrate, which hinders the development of flexible signal processing circuits for multimodal sensors. The circuits that show low power consumption is hardly used for processing high-frequency signals, while the circuits that show high operating speed is not suitable for processing low-frequency signals. For example, the chemical signals obtained from sweat can be detected even at a low operating speed close to direct current,[10] whereas the power consumption should be

Received: October 25, 2022
Accepted: November 21, 2022
Published: December 2, 2022

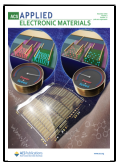

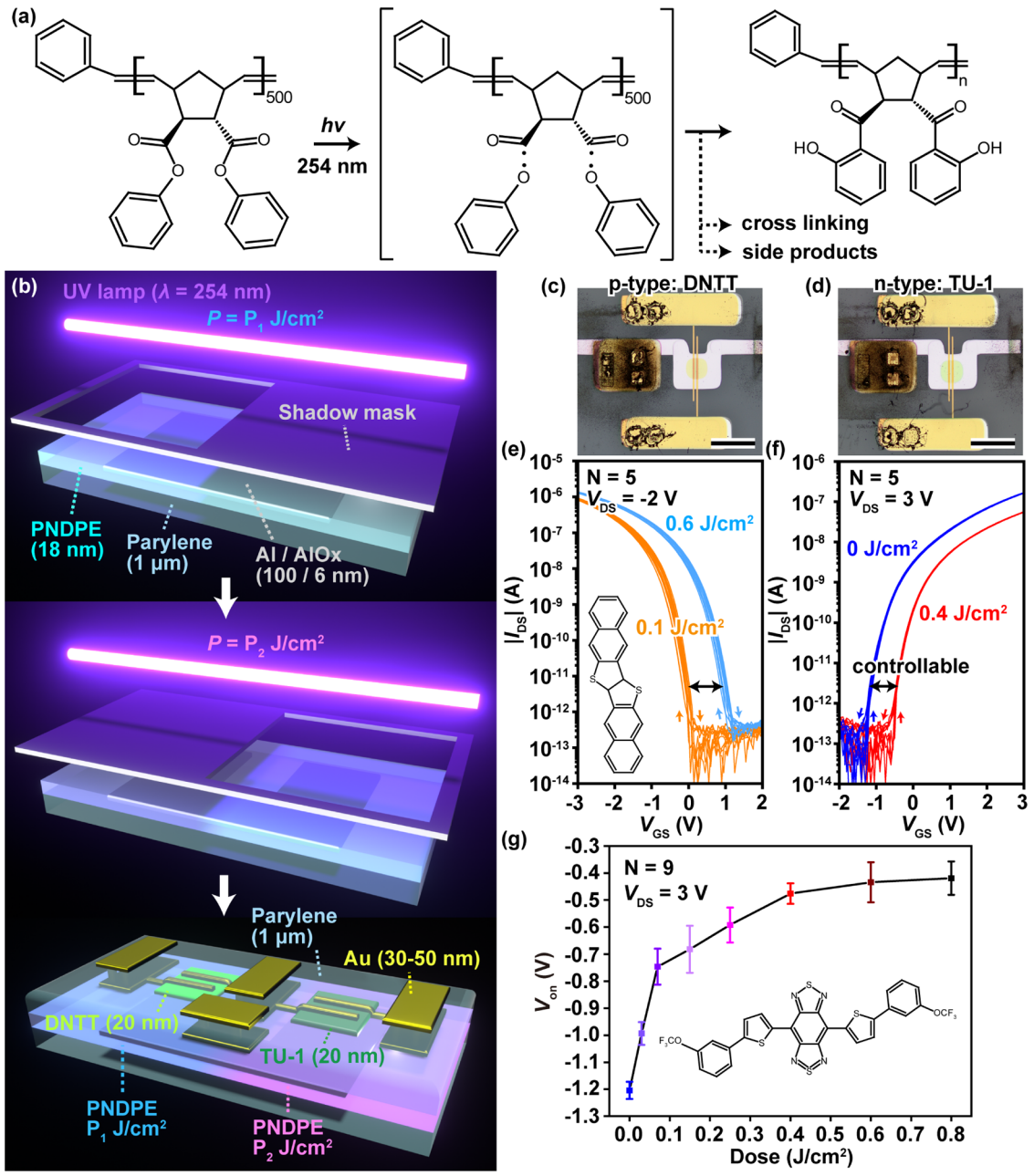

Figure 1. V_{on} shift of the OTFTs with a PNDPE gate dielectric under UV illumination. (a) The photochemical reaction of PNDPE under UV illumination. (b) The device structure of OTFTs and the fabrication process of the organic circuits on a single substrate. The UV dose for the transistors was adjusted using several masks, e.g., P_1 J/cm^2 for p-type transistors and P_2 J/cm^2 for n-type transistors. (c, d) Photographs of the fabricated (c) p-type (DNTT) and (d) n-type (TU-1) OTFTs. Scale bar: 300 μm. (e, f) Forward and reversed transfer curves of the (e) p-type and (f) n-type OTFTs with PNDPE obtained at different UV doses (N = 5). The inset in (e) shows the chemical structure of DNTT. (g) V_{on} of the n-type OTFTs as a function of the UV dose given to the PNDPE film (N = 5). The error bars show the standard deviation. The inset shows the chemical structure of TU-1.

minimized because chemical sensors are often used for long-term monitoring. By contrast, to measure physical signals, such as myoelectricity, the required operating speed of the circuits is several hundreds of hertz.[16] Therefore, it is imperative to develop multimodal sensors with flexible circuits, whose power consumption and operating speeds can be tuned, on a single substrate according to the biosignal type. In addition, with the advent of the Internet of Things (IoT), wearable healthcare devices are expected to be used in large quantities. Thus, it is also important to reduce the manufacturing costs of the devices.

Researchers are now vouching for organic thin-film transistors (OTFTs) for fabricating imperceptible IoT devices with low costs and high material efficiencies because of their intrinsic flexibility and compatibility with the printing process.[1,6,16−19] One of the key fabrication techniques for tuning power consumption and operating speed of the devices is to control the turn-on voltage (V_{on}), which is the voltage needed to reach a certain conductivity, or the threshold voltage (V_{th}), which is the voltage at which a conductive channel is established between the source and drain electrodes, of both the p- and n-type transistors on a single substrate.[20−23] The

https://doi.org/10.1021/acsaelm.2c01444
ACS Appl. Electron. Mater. 2022, 4, 6308−6321

recently demonstrated silicon complementary metal-oxide semiconductor technology allows control of V_{on} or V_{th} via ion implantation in the channel.[24] In the case of OTFTs, V_{on} or V_{th} is controlled by modulating the semiconductor−dielectric interfacial characteristics through self-assembled monolayers, oxygen plasma exposure, and material doping in organic semiconductors.[25−28] However, these methods often require complex patterning processes, because of which tuning the power consumption and operating speed on a single substrate becomes a considerable technological challenge.

Modulating the nanoscale interfacial characteristics of OTFTs by light illumination is a useful method that allows pattern formation on a single substrate using only a shadow mask. The maximum resolution of such a pattern is several hundred nanometers, which is approximately half of the incident light wavelength, and this maximum resolution is sufficiently high for fabricating organic integrated circuits. To date, a few studies have reportedly been conducted on interfacial photochemical reactions using photoreactive insulating polymers.[23,29] However, this seldom-reported polymer-based method is not suitable for fabricating flexible multimodal sensors because of their hysteresis characteristics and high driving voltages.

In this study, a photoreactive insulating polymer poly((±)-endo,exo-bicyclo[2.2.1]hept-ene-2,3-dicarboxylic acid, diphenylester) (PNDPE) was used to finely tune the power consumption and operating speed of ultraflexible organic circuits fabricated on a single substrate. The photopatterning of PNDPE overcomes the trade-off between low power consumption and high operating speed. The V_{on} of the OTFTs shifts when the nanoscale interfacial characteristics of the OTFTs change under UV illumination on PNDPE. The V_{on} shift occurs only where the UV radiation illuminates PNDPE, and the amount of V_{on} shift depends on the UV dose. This suggests that the photopatterning can tune the power consumption and operating speed of the complementary circuits one-by-one on a single substrate. In other words, for low-frequency signals, low-power circuits can be assigned for signal processing, whereas for high-frequency signals, high-speed circuits can be assigned on a single substrate by UV-photopatterning of PNDPE. PNDPE forms a dense, homogeneous, and ultrathin film that aids in the fabrication of high-performance organic transistors.[30−34] In addition, PNDPE can be synthesized in large quantities (several grams) with a more than 70% yield on a laboratory scale and used for solution-based processes with nonhalogenated solvents. The nanoscale interfacial characteristics of OTFTs are typically modulated via the photo-Fries rearrangement of an aromatic ester into hydroxy ketone upon ultraviolet (UV) illumination without photoinitiators. In our previous study, we demonstrated a method to control the V_{th} of p-type OTFTs to obtain high-performance organic unipolar circuits.[33] In this study, we demonstrated the fine-tuning of both the power consumption and operating speed of ultraflexible organic complementary circuits as well as the V_{on} of n-type OTFTs, fabricated on a single substrate, through a nanoscale interfacial photochemical reaction of PNDPE. The complementary inverters and ring oscillators were fabricated on a large area (6 cm × 10 cm) and an ultraflexible (total thickness < 2.4 μm) single substrate. The V_{on} of n-type OTFTs was controlled from −1.2 to −0.4 V with a standard deviation in the range from 32 to 87 mV by changing the UV dose. Time-of-flight secondary ion mass spectrometry (TOF-SIMS) analysis of the fabricated circuits was conducted, and the corresponding results implied that the V_{on} of the OTFTs, fabricated on a single substrate, is controlled one-by-one by patterning the UV-illuminated area and that the V_{on} shift is correlated to the interfacial photochemical reaction. The power consumption was tuned by a factor of 6 such that the minimum static power consumption was 30 ± 9 pW at transient and 4 ± 1 pW at standby. The operating speed was tuned by a factor of 4, such that the minimum stage delay time was of the order of hundreds of microseconds at a supply voltage of 2.5 V. The fabricated inverters were operated at 0.2 V, indicating that these devices can be operated using various energy sources, such as biofuel cells. Furthermore, we demonstrated electromyogram (EMG) measurements with PNDPE, suggesting that the nanoscale interfacial photochemical reaction for OTFTs can be used for tuning the circuit performances according to the target biosignals. The nanoscale interfacial photochemical reaction with PNDPE demonstrated in this study will contribute to the development of imperceptible and wearable multimodal sensors with organic signal processing circuits for long-term monitoring with minimized power consumption.

RESULTS AND DISCUSSION

Figure 1a illustrates the UV-induced photochemical reaction of PNDPE, which was synthesized by a ring-opening metathesis polymerization process (the detailed synthesis process is reported elsewhere[35]). As shown in Figure 1a, the UV illumination of PNDPE radicalizes the aromatic ester in its side chain, followed by the photo-Fries rearrangement of the ester into hydroxy ketones, cross-linking and other side products such as phenol.[30,35] These rearranged hydroxy ketones or side products cause the V_{on} shift of the transistors.[30] Figure 1b shows the schematic of the UV patterning process and structures of the p- and n-type bottom-gated top-contact transistors fabricated on a single substrate. A 1-μm-thick parylene (diX-SR) film was used as the substrate because of the ultraflexibility and biocompatibility of parylene.[7,36,37] First, aluminum was thermally evaporated to form an anodized 6-nm-thick aluminum oxide layer. Then, a solution of PNDPE (10 mg/mL) dissolved in anisole was spun to form a gate dielectric of 18 ± 1.4 nm thickness. The thickness of the PNDPE gate dielectric was confirmed by surface profile measurements (number of samples, N = 15) (Figure S1, Supporting Information). This PNDPE gate dielectric was illuminated by a handy-type Hg lamp (peak wavelength, λ_p = 254 nm) through metal masks. To control the interfacial photochemical reaction of the transistors on a single substrate, the UV dose was adjusted using several masks, e.g., P_1 J/cm^2 for p-type transistors and P_2 J/cm^2 for n-type transistors. The gate dielectrics were illuminated by UV light under a nitrogen gas atmosphere to suppress any ozone-induced damage. Then, a 20-nm-thick layer of dinaphtho[2,3-*b*:29,39-*f*]thieno[3,2-*b*]thiophene (DNTT; p-type semiconductor) and a 20-nm-thick layer of 4,8-Bis[5-[3-(trifluoromethoxy)phenyl]-2-thienyl]-2$\lambda^4\delta^2$-benzo[1,2-*c*:4,5-*c*′]bis[1,2,5]thiadiazole (TU-1, benzobis(thiadiazole) derivative; n-type semiconductor),[38] were deposited at different positions on the substrate, and gold source−drain (SD) electrodes were deposited via thermal evaporation. Subsequently, the transistors were passivated by a 1-μm-thick diX-SR to improve their air stability and to sandwich the transistors at a neutral strain position. Finally, the contact pads for measurements were extracted via holes. The detailed fabrication process is described in the Methods section

https://doi.org/10.1021/acsaelm.2c01444
ACS Appl. Electron. Mater. 2022, 4, 6308−6321

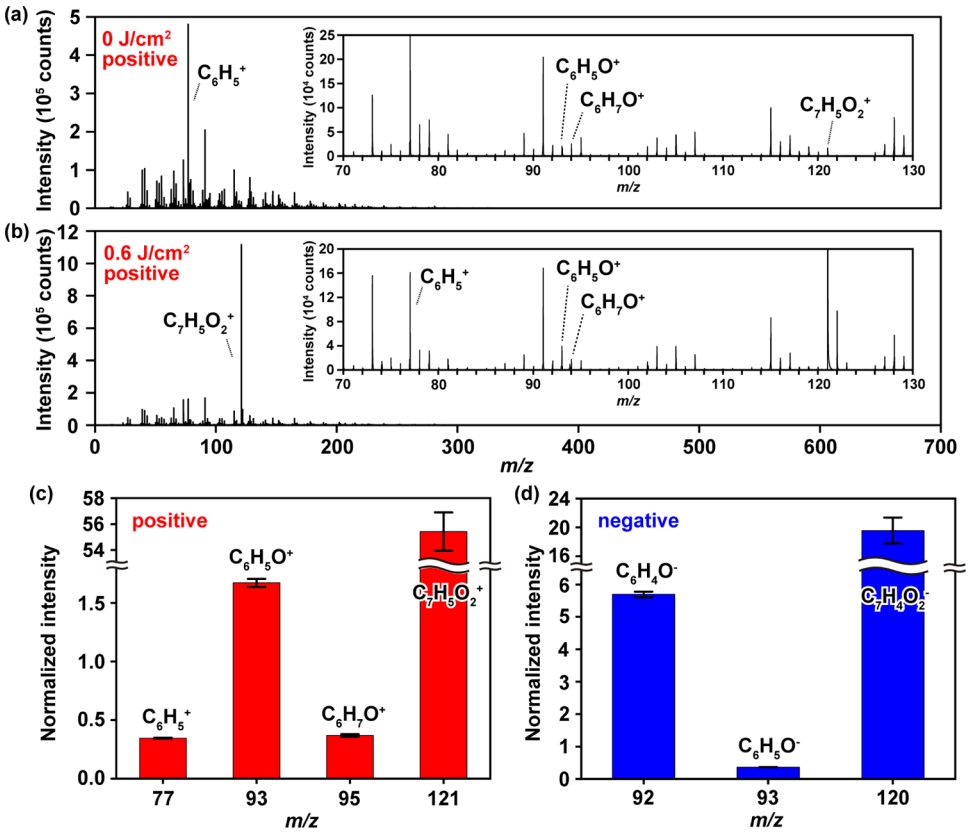

Figure 2. Chemical analysis of the PNDPE film by TOF-SIMS. (a, b) Mass spectra of the positive secondary ions obtained from the PNDPE film (a) with and (b) without UV illumination in the range from m/z = 0 to 700. The insets in (a, b) show the expanded mass spectra in the range from m/z = 70 to 130. The mass spectra were obtained by integrating the total ion counts of the scanned area. (c, d) Normalized intensity of the (c) positive and (d) negative fragment ions. The intensity obtained from the UV-illuminated PNDPE film was normalized by that of the film without UV illumination. The error bars show the standard deviations.

and Figure S2 (Supporting Information). The total device thickness was less than 2.4 μm. Figure 1c,d shows the photographs of the fabricated p- and n-type transistors, in which the channel length and width were 14 and 140 μm, respectively. The area of the gate electrode, organic semiconductor, and SD electrode was minimized to reduce their overlapping. The gate electrode−semiconductor and gate−SD electrode overlapping areas were 0.022 and 0.0032 mm^2, respectively.

Figure 1e,f shows the transfer curves of the p- and n-type transistors. The electrical characteristics of the transistors were measured in air as well as under dark conditions at room temperature (unless otherwise stated). The transfer curves showed that the V_{on} of the p- and n-type transistors were tuned by changing the UV dose. As a result of the UV illumination, the V_{on} of the fabricated transistors changed such that the p-type transistors converted from enhancement mode toward depletion mode (details of the p-type transistor characteristics are described in our previous report[33]), while the n-type ones showed the opposite characteristics (i.e., depletion mode toward enhancement mode conversion). The change in V_{on} upon UV illumination possibly originated from an increase in the number of electron traps at the interface because of the formation of hydroxy ketones or the generation of dipoles in the PNDPE gate dielectric film.[30,33,39] In the case of p-type transistors, deep electron traps or dipoles generate additional hole carriers, which contribute to the positive V_{on} shift of the p-type transistors. The density of traps at the interface between DNTT and PNDPE was investigated in our previous study, in which UV illumination was found to increase the density of these traps.[30,33] Similarly, in the case of n-type transistors, it is expected that the deep electron traps and/or dipoles suppress the electron carriers in the semiconductor, thereby contributing to the observed V_{on} shift of the n-type transistors toward enhancement. A negligible hysteresis was observed in both the p- and n-type transistors at the source−drain voltage, V_{DS} = −2 and 3 V, respectively, even though the transistors were operated in air. The n-type transistors exhibited high bias-stress stability at low gate voltages; the source−drain current (I_{DS}) was reduced by 3 and 6% for the nonilluminated and illuminated n-type transistors at the supply voltage, V_{dd} = 0.5 V (Figure S3, Supporting Information). The off-currents were less than a few picoamperes, both with and without UV illumination, and the on/off ratios were high (~5−6). The small off-current and high on/off ratio can be attributed to the modulation of the carriers only at the semiconductor−dielectric interface, which is different from bulk doping in organic semiconductors.[27] As shown in Figure S4 (Supporting Information), the gate current was very small, i.e., of the order of several picoamperes or less. The mobility decreased from 1.8×10^{-2} to 6.0×10^{-3} cm^2 V^{-1} s^{-1} upon UV illumination (Figure S5, Supporting Information).

The V_{on} of the n-type transistor was precisely controlled by changing only the UV dose. We investigated the relation between V_{on} and the UV dose, and the corresponding results are shown in Figure 1g. Evidently, V_{on} varied from −1.2 to

https://doi.org/10.1021/acsaelm.2c01444
ACS Appl. Electron. Mater. 2022, 4, 6308−6321

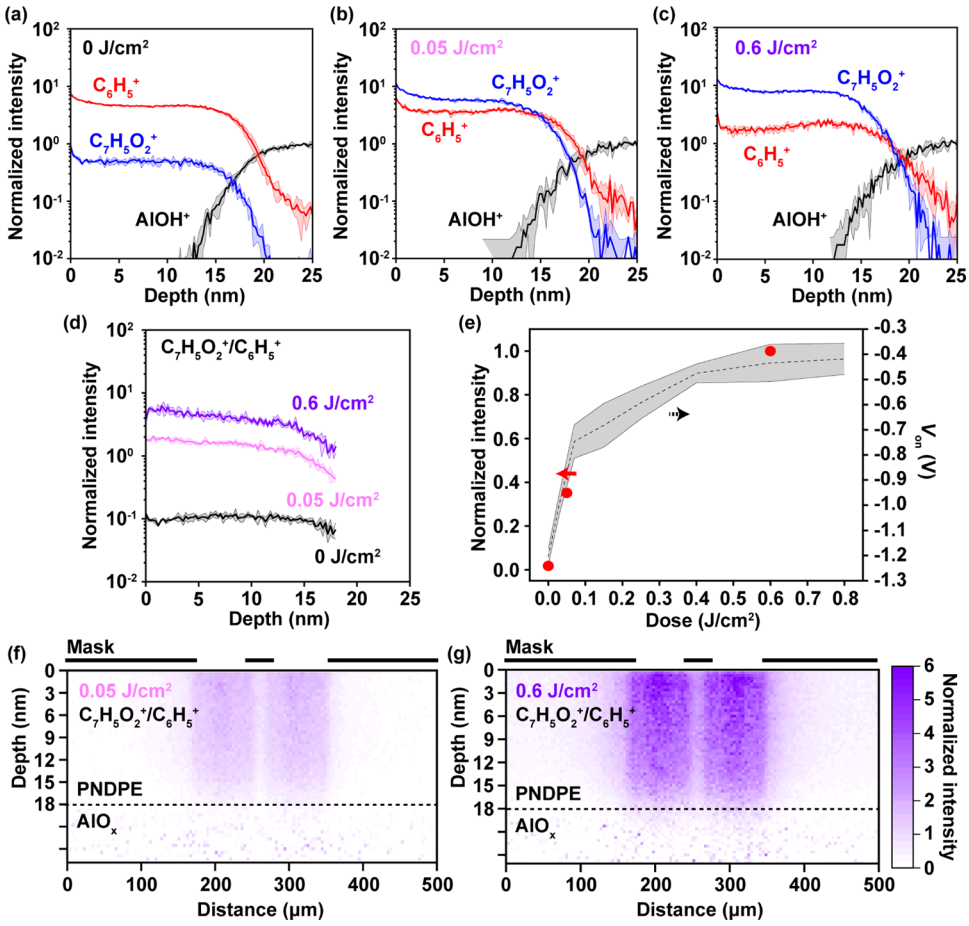

Figure 3. Cross-sectional TOF-SIMS analysis of the PNDPE film. (a–c) The depth profile of the $C_6H_5^+$, $C_7H_5O_2^+$, and $AlOH^+$ fragment ions in the PNDPE film with a UV dose of (a) 0 J cm^{-2}, (b) 0.05 J cm^{-2}, and (c) 0.6 J cm^{-2}, respectively. The intensity of each fragment ion was normalized by that of the $AlOH^+$ fragment ion. The colored areas show the standard deviations. Here, the profiles for depths >18 nm do not reflect the actual situation because, in these cases, the AlO_x layer was etched only negligibly. (d) The depth profile of the normalized $C_7H_5O_2^+/C_6H_5^+$ intensity in the PNDPE film at different UV doses. The colored areas show the standard deviations. (e) The normalized $C_7H_5O_2^+/C_6H_5^+$ intensity at a depth of 0–3 nm as a function of the UV dose. The V_{on} value, which is the same as that in Figure 1g, is also shown for comparison. The colored areas show the standard deviations. (f, g) Cross-sectional images of the normalized $C_7H_5O_2^+/C_6H_5^+$ intensity in the PNDPE film and at the PNDPE–AlO_x interface at the UV dose of (f) 0.05 J cm^{-2} and (g) 0.6 J cm^{-2}.

−0.4 V at V_{DS} = 3 V when the UV dose was changed from 0 to 0.8 J/cm^2. The in-plane standard deviation was in the range of 32–87 mV. The shelf-life stability measurements indicated that the deviation of the V_{on} of the n-type transistor was less than 250 mV over 90 days (Figure S6, Supporting Information). V_{on} drastically changed at the initial UV illumination, and then the V_{on} shifts gradually saturated with the increasing UV dose; these results are consistent with those observed for the p-type transistors.[33]

To investigate the surface properties of the photochemically (UV illumination) reacted PNDPE as well as to assess whether the UV-illuminated pattern expanded with the increasing UV dose, the PNDPE film was analyzed by TOF-SIMS. TOF-SIMS is a powerful tool and suitable for investigating the chemical properties of polymer gate dielectrics because it can distinguish the properties of a film surface, which forms a semiconductor–dielectric interface, from that in a film, which is ineffective for OTFT's characteristics. First, mass spectra were measured to understand whether the intensities of fragment ions changed by UV illumination. Figure 2a,b shows the mass spectra of the positive secondary ions at the surface of the PNDPE film, both with and without UV illumination, in the range from m/z = 0 to 700. The insets in Figure 2a,b show the expanded mass spectra in the range from m/z = 70 to 130. For the TOF-SIMS measurements, Bi_3^{++} ions were used as the primary ions owing to their suitability for the analysis of organic molecules. Details of the measurement setup are described in the Methods section. Considering the chemical structure of PNDPE, the peaks at m/z = 93, 95, and 121 observed in the mass spectra can be ascribed to the $C_6H_5O^+$, $C_6H_7O^+$, and $C_7H_5O_2^+$ ions, respectively. These ions were possibly formed by the fragmentation of the carbonyl α-cleavage in the side chain of PNDPE. In addition, a peak at m/z = 77 was observed, which might have originated from a $C_6H_5^+$ ion. The $C_6H_5^+$ ions were possibly partially formed by the fragmentation of the cleavage at the aromatic ester in the PNDPE film without UV illumination and partially by the OH bond cleavage and α-cleavage in the UV-illuminated PNDPE film. The negative secondary ion mass spectra shown in Figure S7 (Supporting Information) indicate the formation of $C_6H_4O^-$ (m/z = 92), $C_6H_5O^-$ (m/z = 93), and $C_7H_4O_2^-$ (m/z = 120) ions. We compared the intensities of the peaks corresponding to these fragment ions obtained from the PNDPE film with and without UV illumination, and the results

https://doi.org/10.1021/acsaelm.2c01444
ACS Appl. Electron. Mater. 2022, 4, 6308–6321

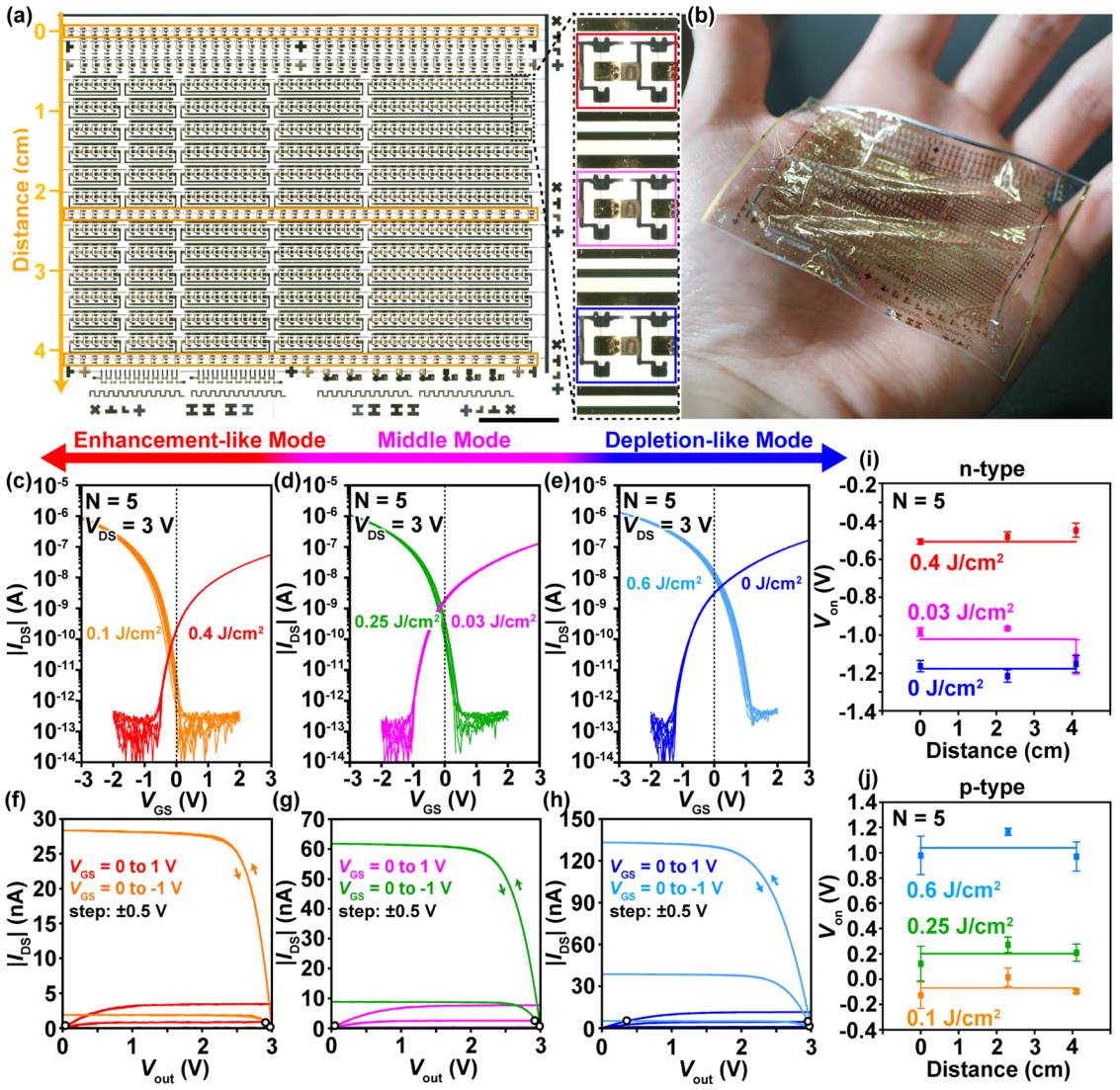

Figure 4. Characteristics of the OTFTs fabricated on a single substrate. (a) A photograph of the 1341 OTFTs that include 72 inverters and 60 ring oscillators (24 5-stage, 24 9-stage, and 12 17-stage) fabricated on a single substrate. The transistor TEGs are marked using orange squares. The red, pink, and blue squares, representing the "enhancement-like mode," "middle mode," and "depletion-like mode" inverters, respectively, indicate that the complementary inverters showed different characteristics at different UV doses given to the PNDPE film. Scale bar: 10 mm. (b) A photograph of the ultraflexible device. (c–e) Forward and reversed transfer curves of the p- and n-type OTFTs indicate that the performances of the complementary inverters can be tuned by varying the UV doses: (c) p-type: 0.1 J cm^{-2}, n-type: 0.4 J cm^{-2}; (d) p-type: 0.25 J cm^{-2}, n-type: 0.03 J cm^{-2}; and (e) p-type: 0.6 J cm^{-2}, n-type: 0 J cm^{-2}, (N = 5). (f–h) Forward and reversed output characteristics of the p- and n-type OTFTs. The UV dose is the same as that described in (c)–(e). (i, j) V_{on} of the (i) n-type and (j) p-type OTFTs as a function of the fabrication position (N = 5).

are plotted in Figure S8 (Supporting Information). Figure 2c,d shows the intensities of the fragment ions obtained from the UV-illuminated PNDPE, normalized by those obtained from the non-UV-illuminated PNDPE. The normalized intensity of the $C_7H_5O_2^+$ ion peak was 55. One of the possible reasons for the intensity difference is the ionization efficiency of fragment ions; for instance, salicylaldehyde shows the reference peak at m/z = 122 (molecular ion), while phenylacetate shows the reference peak at m/z = 93 (ascribed as a $C_6H_5O^+$ ion).[40] The ionization efficiency also depends on matrix effects and the ease of vaporization of the fragment ions. The normalized intensities of the $C_6H_5^+$, $C_6H_5O^+$, and $C_6H_7O^+$ ion peaks were 0.35, 1.7, and 0.37, respectively. In terms of negative secondary ions, the normalized intensities of the $C_6H_4O^-$, $C_6H_5O^-$, and $C_7H_4O_2^-$ ion peaks were 5.7, 0.36, and 20, respectively.

Furthermore, the photochemically reacted PNDPE film was etched by Ar-ion clusters, and the corresponding depth profiles and cross-sectional images were analyzed to evaluate the surface properties of the films at the nanoscale. We focused on the $C_7H_5O_2^+$ and $C_6H_5^+$ ions, whose intensity ratios showed the largest increment and decrement under UV illumination, respectively. Figure 3a–c shows the depth profiles of the $C_7H_5O_2^+$, $C_6H_5^+$, and $AlOH^+$ ions at different UV doses. The corresponding intensities were normalized by the points where the intensity of the $AlOH^+$ ion signal was almost constant. When the UV dose was increased, the normalized intensities of the $C_7H_5O_2^+$ and $C_6H_5^+$ ion signals increased and decreased, respectively, across the PNDPE–AlO_x interface. Here, we considered a depth of 18 nm, where the normalized intensity of the $AlOH^+$ ion signal was approximately 0.5. Additionally, the profiles for depths >18 nm did not reflect the actual

https://doi.org/10.1021/acsaelm.2c01444
ACS Appl. Electron. Mater. 2022, 4, 6308–6321

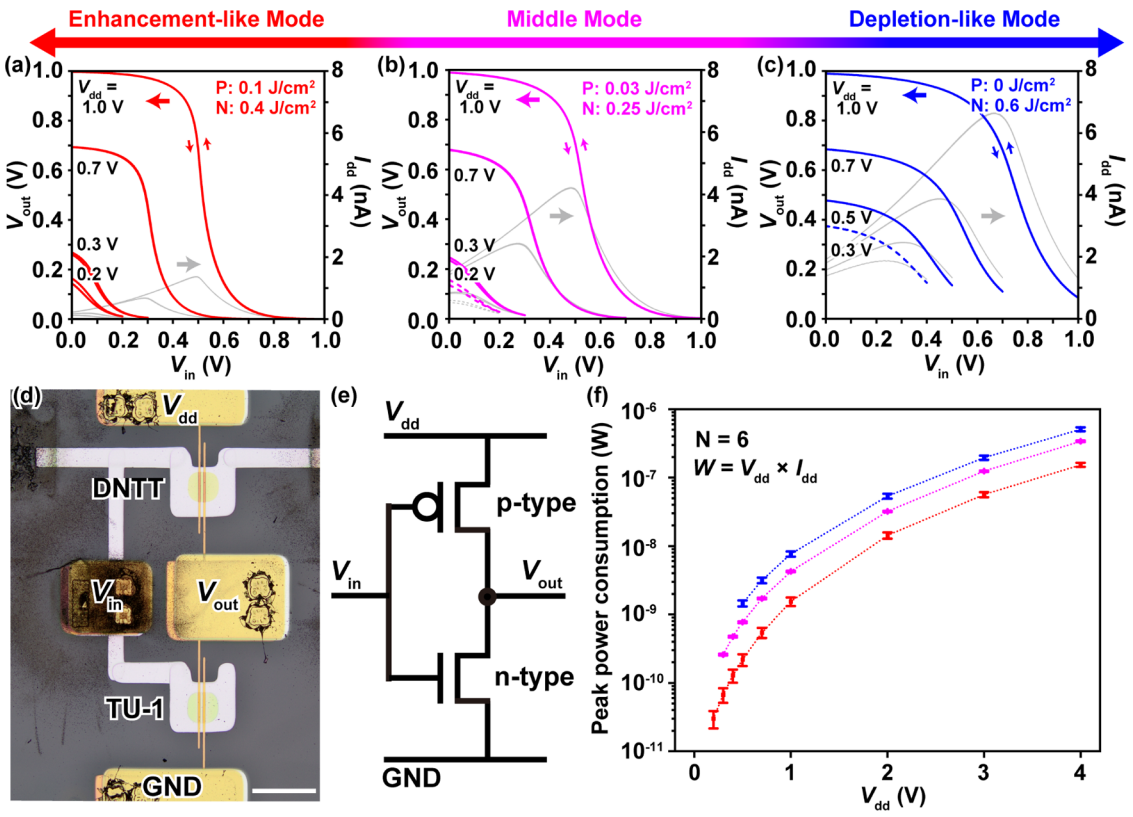

Figure 5. Performance of the complementary inverter at different UV doses given to the PNDPE film (different modes). (a–c) Forward and reversed inverter characteristics obtained by varying the UV dose: (a) p-type: 0.1 J cm^{-2}, n-type: 0.4 J cm^{-2}; (b) p-type: 0.25 J cm^{-2}, n-type: 0.03 J cm^{-2}; and (c) p-type: 0.6 J cm^{-2}, n-type: 0 J cm^{-2}. (d) The device photo of the complementary inverter. Scale bar: 300 μm. (e) The circuit diagram of the complementary inverter. (f) Peak power consumption of the complementary inverter at different doses as a function of V_{dd} (N = 6). The error bars show the standard deviations.

situation because the AlO_x layer was only negligibly etched during these measurements. The observed steep increase in the signal intensity near the surface can be attributed to the measurement conditions, such as the difference in the concentration of the Ar-ion clusters during the initial and final sputtering.

To evaluate the progress of the photochemical reaction of PNDPE as the influence of the intensity changes caused by the measurement conditions was suppressed, we calculated the $C_7H_5O_2^+/C_6H_5^+$ intensity ratio. As shown in Figure S9 (Supporting Information), the depth profiles of the $C_6H_7O^+$ ion, whose signal intensity decreased with UV illumination, and that of the $C_6H_5^+$ ions were found to be almost uniform across the PNDPE film when the corresponding intensities were normalized by the intensity of the $C_6H_5^+$ ion signal. This result suggests that normalization can reduce the influence of intensity changes caused by the measurement conditions. Figure 3d shows that the normalized $C_7H_5O_2^+/C_6H_5^+$ ion signal intensity obtained from the vicinity of the UV-illuminated film surface was dependent on the depth of the PNDPE film, while a negligible dependence of this intensity ratio was observed for the non-UV-illuminated film. The intensity obtained from the film with 0–3-nm-deep etched profiles was 1.7 times higher than that obtained from the film with 12–15-nm-deep profiles (Figure S10, Supporting Information). Figure 3e compares the normalized $C_7H_5O_2^+/C_6H_5^+$ ion signal intensity with the V_{on} shift of the n-type transistors as a function of the UV dose. The steep increase in the normalized intensity between 0 and 0.05 J is consistent with the steep change in V_{on}. Based on these observations, it can be stated that the photochemical reaction progressed more near the PNDPE surface, i.e., the reaction rate of the film with 12–15-nm-deep is 60% when the one with 0–3-nm-deep is defined as 100%, and that the V_{on} shift is correlated to the interfacial photochemical reaction. We further investigated the photochemical reaction of the PNDPE film from depth profile imaging. As shown in Figure S11 (Supporting Information), PNDPE was illuminated through a patterned metal mask. Figure 3f,g shows the cross-sectional images obtained by summing the $C_7H_5O_2^+/C_6H_5^+$ ion signal intensities emitted from a 500 μm × 200 μm area. In the cross-sectional images without normalization, as shown in Figure S12 (Supporting Information), the contrast between the illuminated and nonilluminated areas is clearly visible, indicating that the photochemical reaction occurred only in the illuminated area. In addition, we confirmed that the photochemical reaction progressed in the vicinity of the surface with the increasing UV dose, which is consistent with the depth profile, and that the UV-illuminated pattern near the surface did not significantly expand with the increasing dose. In other words, the photochemical reaction that shifts the V_{on} of the transistors occurred mostly within the UV-illuminated area near the surface at the nanoscale. Therefore, it can be inferred that the V_{on} of the OTFTs, fabricated on a single substrate, is controlled one-by-one by patterning the UV-illuminated area.

To demonstrate that the performances of the ultraflexible organic integrated circuits can be tuned by the nanoscale interfacial photochemical reaction, we fabricated complemen-

https://doi.org/10.1021/acsaelm.2c01444
ACS Appl. Electron. Mater. 2022, 4, 6308–6321

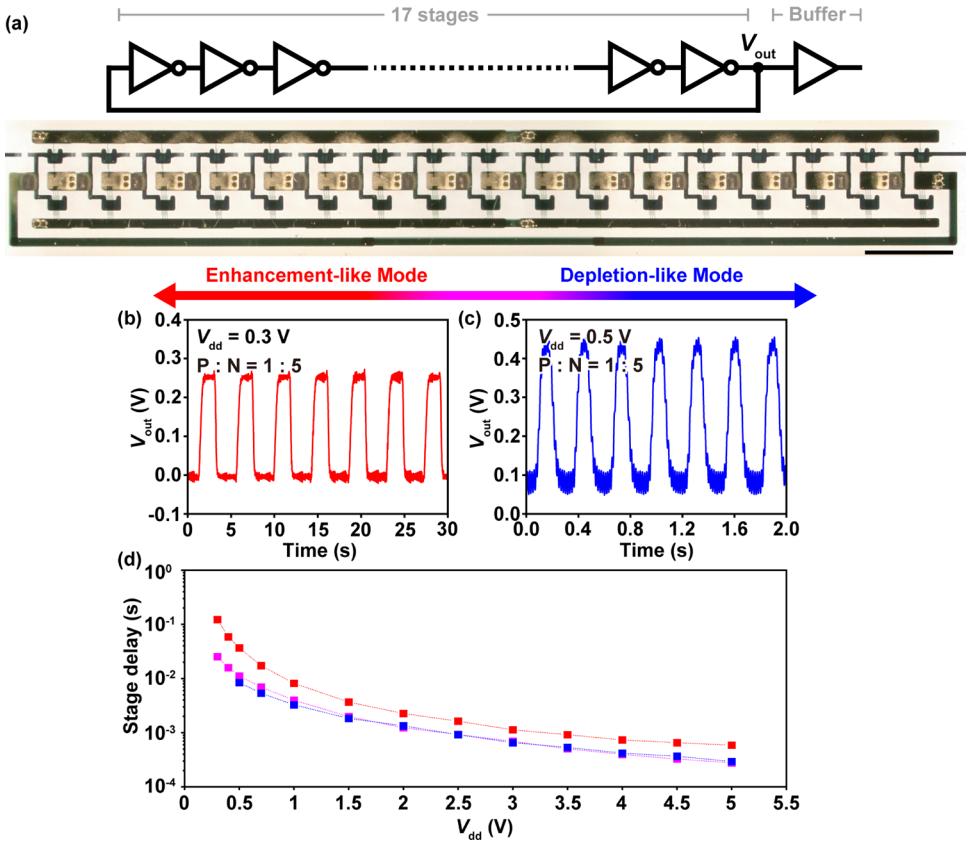

Figure 6. Performance of the ring oscillator at different UV doses given to the PNDPE gate dielectric (different mode). (a) The schematic circuit diagram of the ring oscillator and an external buffer, and the device photo of the 17-stage ring oscillator (channel width; p-type/n-type = 1:5). Scale bar: 2 mm. (b, c) Output waveforms of the (b) "enhancement-like mode" and (c) "depletion-like mode" ring oscillators. (d) Stage delay of the ring oscillator, with different modes, as a function of V_{dd}.

tary inverters and ring oscillators on a single substrate. Complementary inverters are essential building blocks for analogue and digital circuits because their static power consumption is lower than that of unipolar inverters. Ring oscillators are required for generating clock signals and are thus useful for developing devices such as matrix arrays. Figure 4a shows an optical image of the fabricated devices. In total, 1341 transistors consisting of 117 test element groups (TEGs), 72 inverters, and 60 ring oscillators (24 5-stage, 24 9-stage, and 12 17-stage) were fabricated over a large 6 cm × 10 cm substrate. The inverters displayed in red, pink, and blue squares in the expanded image showed different characteristics. The details of the fabrication conditions are depicted in Figure S13 (Supporting Information). As shown in Figure 4b, the circuits were fabricated on an ultraflexible and biocompatible parylene substrate, making them suitable for application in imperceptible biosensors. Figure 4c–e shows the transfer curves of the p- and n-type transistors, which constituted complementary inverters with three different characteristics. The V_{on} of the transistors was controlled using five differently patterned metal masks and by varying the UV dose. In the "enhancement-like mode" inverters, the UV doses for the p- and n-type transistors were 0.1 and 0.4 J/cm^2, respectively, so that the V_{on} of both transistor types was close to 0 V. V_{on} = 0.01 and −0.48 V in p- and n-type transistors, respectively. This configuration suppressed the power consumption of the inverters. On the contrary, in the "depletion-like mode" inverters, the UV doses for p- and n-type transistors were 0.6 and 0 J/cm^2, respectively, to realize a V_{on} that enabled both types of transistors to operate in depletion mode. V_{on} = 1.2 and −1.2 V in p- and n-type transistors, respectively. In this configuration, the operating speed of the inverters improved significantly. Therefore, Figure 4c–e indicates that the V_{on} shift originating from the photopatterning of PNDPE can be utilized to tune the power consumption and operating speed of inverters on a single substrate. To simulate the input/output characteristics of the complementary inverters, the output curves of the p- and n-type transistors were measured at different doses, as shown in Figure 4f–h. The output curves of the n-type transistors are plotted as the output voltage, $V_{out} = V_{DS}$, and those of the p-type transistor are plotted as $V_{out} = V_{dd} - V_{DS}$. In these figures, both transistor types show linear characteristics in the nonsaturated regime, which is preferred for deducing the rail-to-rail characteristics of the inverters.[41] The expected output voltage and through-current of the inverter are shown by black circles, indicating the rail-to-rail characteristics of the "enhancement-like mode" and "middle mode" inverters. Figure 4i,j presents the dependence of the V_{on} of both transistor types on which position the transistors are fabricated within the substrate. The transistor TEGs were fabricated on the upper, center, and bottom parts of the substrate, as displayed in the orange squares in Figure 4a. The V_{on} of both transistor types showed no significant dependence on the fabricated position on a single substrate. The maximum standard deviations of V_{on} for the n- and p-type transistors were approximately 130 and 190 mV, respectively. Notably, the deviation in V_{on} can be attributed to the handy-type lamp

https://doi.org/10.1021/acsaelm.2c01444
ACS Appl. Electron. Mater. 2022, 4, 6308−6321

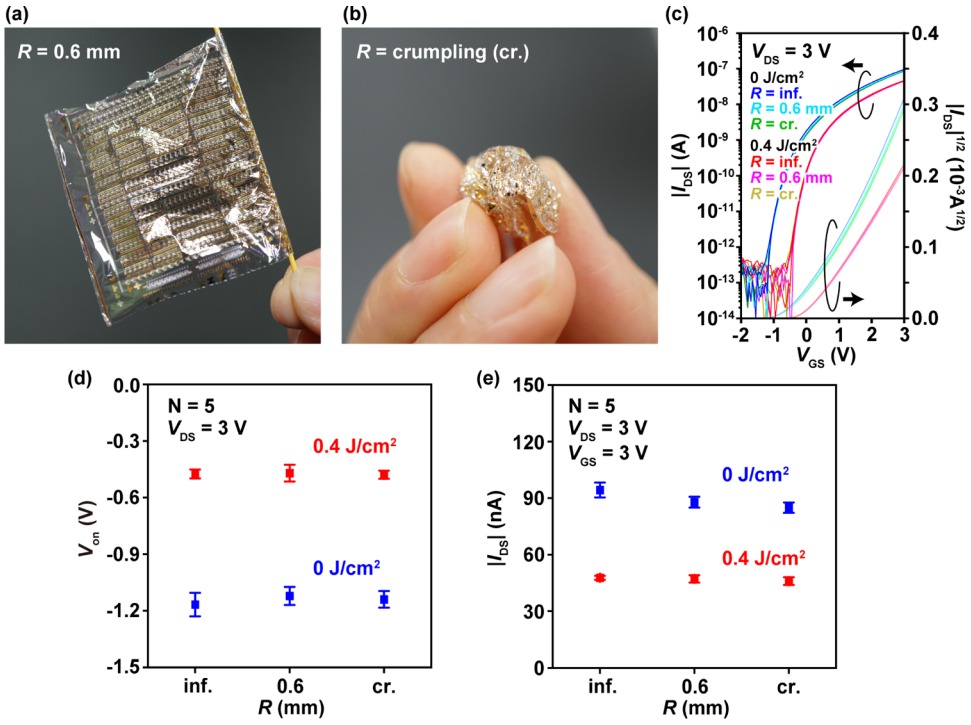

Figure 7. Mechanical flexibility test of the n-type OTFTs. The device photo of (a) the OTFT rolled up along a cylinder with a radius of 0.6 mm (R = 0.6 mm) and (b) the crumpled (R = crumpling) OTFT. (c) Forward and reversed linear- and log-scale transfer characteristics of the n-type transistor with and without UV illumination of the PNDPE film obtained for each bending test. (d) The V_{on} and (e) I_{DS} plots of n-type OTFTs at different UV doses for PNDPE under each bending test.

that radially irradiated the UV light on the films. Therefore, the deviation in V_{on} can be reduced using a collimated light source.

We first demonstrated the tuning of the power consumption by fabricating inverters with different operating modes. We measured the characteristics of the complementary inverters at different V_{dd}, as shown in Figure 5a–c. The operated inverter characteristics are shown using solid lines in Figure 5a–c. The device photo and circuit diagram of the inverter are shown in Figure 5d,e. Negligible hysteresis was observed in the supply voltage. The gray lines in Figure 5a–c show the through-currents at V_{dd}. Figure 5f summarizes the power consumption at the peak through-current calculated from six inverters. The power consumption of the "enhancement-like mode," "middle mode," and "depletion-like mode" inverters at V_{dd} = 0.5 V were 220 ± 46 pW, 770 ± 21 pW, and 1.45 ± 0.14 nW, respectively, indicating that the power consumption was tuned by a factor of approximately 6. Moreover, at V_{dd} = 0.2 V, the minimum static power consumption was 30 ± 9 pW at transient and 4 ± 1 pW at standby when the "enhancement-like mode" inverters (N = 6) were used. To the best of our knowledge, this power consumption is the lowest among those of the previously reported flexible organic complementary inverters that include polymer gate dielectrics (Table S1, Supporting Information). In this study, the inverter was assumed to operate such that the noise margin could be found by the "maximum equal criterion" (Figure S14, Supporting Information).

The minimum driving voltages for the "enhancement-like mode," "middle mode," and "depletion-like mode" inverters were 0.2, 0.3, and 0.5 V, respectively. Because of these low driving voltages, a variety of energy sources, such as biofuel cells, can be used to drive these devices for a plethora of applications.[42] The difference between the minimum driving voltages of the inverters with different modes can be attributed to the change in the resistive divider ratio of the transistors. This implies that the resistive dividing ratio can be finely tuned by controlling V_{on}. The "enhancement-like mode" and "middle mode" inverters almost showed a rail-to-rail operation, whereas the "depletion-like mode" inverters did not show rail-to-rail characteristics, which can also be attributed to the change in the resistive dividing ratio. The trip point of the fabricated inverters showed small deviations; all of the fabricated inverter characteristics are shown in Figure S15 (Supporting Information). The gains of the "enhancement-like mode," "middle mode," and "depletion-like mode" inverters were 34, 22, and 14, respectively, at V_{dd} = 4 V (Figure S16, Supporting Information).

Furthermore, the operating speeds of the inverters and ring oscillators could be tuned using inverters with different operating modes. We measured the stage delay of the ring oscillators, i.e., the delay time per inverter. Figure 6a shows the circuit diagram and optical image of a 17-stage ring oscillator. We fabricated a variable channel width in the n-type transistors (140, 420, 700, and 1120 μm), and the transistor with a channel width of 700 μm (channel width; p-type/n-type = 1:5) is shown in Figure 6a. Varying the channel width of the n-type transistors did not produce significant deviation in their V_{on}, as shown in Figure S17 (Supporting Information). Figure 6b,c shows the output waveforms of the ring oscillators consisting of the "enhancement-like mode" and "depletion-like mode" inverters, respectively. The ring oscillators were passivated with a metal encapsulation layer to evaluate their performance under more stable conditions. The oscillations were observed even at low supply voltages of 0.3 and 0.5 V for the "enhancement-like mode" and "depletion-like mode" inverters, respectively, with an almost rail-to-rail swing. The n-type transistors with different channel widths also showed

https://doi.org/10.1021/acsaelm.2c01444
ACS Appl. Electron. Mater. 2022, 4, 6308–6321

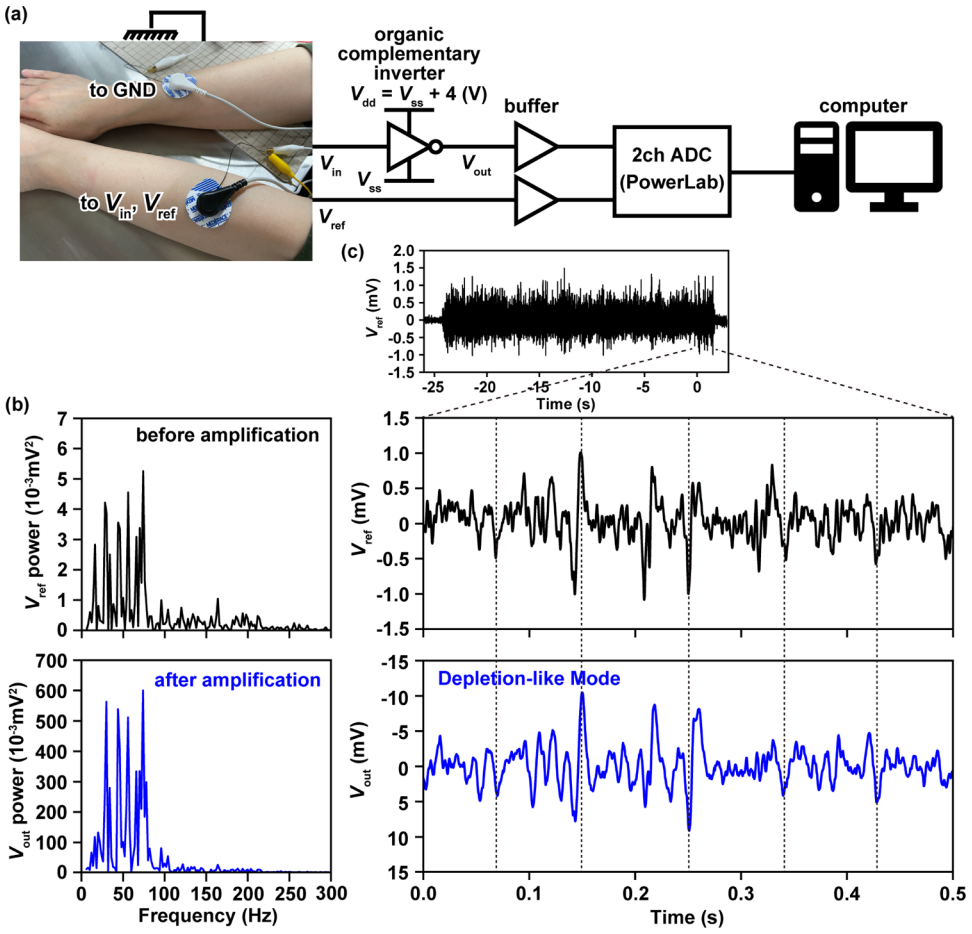

Figure 8. EMG measurements using a complementary organic inverter. (a) The experimental setup to measure EMG signals from the arms of the subject, a healthy woman. One of the two electrodes was for V_{in} and V_{out}, and the other was connected to the ground (GND). A "depletion-like mode" inverter was used as the amplifier. (b) Power spectra of the EMG signals before and after the amplification. (c) Reference and output EMG waveforms before and after the amplification. The dotted vertical lines represent the peaks of the EMG signals and confirm the relation between the two signals. The compound action potentials were extracted by squeezing the muscles.

oscillations, as shown in Figure S18 (Supporting Information). The oscillation frequency increased as the channel width increased because of the larger transconductance of the n-type transistors.

Figure 6d shows the relationship between the stage delay and V_{dd} of the "enhancement-like mode," "middle mode," and "depletion-like mode" ring oscillators (channel width; p-type/n-type = 1:5). The stage delay was systematically tuned by controlling the V_{on} of the transistors. The stage delay t_d was calculated as $t_d = 1/(2Nf)$, where N is the number of inverter stages and f is the measured oscillation frequency. It was observed that at V_{dd} = 0.5 V, the "enhancement-like mode," "middle mode," and "depletion-like mode" ring oscillators showed stage delays (oscillation frequencies per stage) of 37 ms (14 Hz), 11 ms (45 Hz), and 8.4 ms (59 Hz), respectively. Thus, the operating speed was tuned by a factor of approximately 4. The "depletion-like mode" ring oscillator showed the smallest stage delay, mainly because of the largest transconductance of the transistors. This phenomenon can be explained by the theory reported by Zschieschang et al., who mention that the stage delay of a ring oscillator is inversely proportional to the transconductance of transistors.[21] Because the transconductance increases with the absolute value of $V_{GS} - V_{on}$, the depletion-mode transistors, which have the maximum absolute value of $V_{GS} - V_{on}$ at a certain V_{GS}, show the largest transconductance. At V_{dd} = 2.5 V, the stage delay of the "depletion-like mode" ring oscillators was 919 μs, suggesting that the complementary circuits can be applied to physical signal measurements, such as in electromyography. The yields of the ring oscillators fabricated on three substrates were high: the yields were 93.1% (67 of 72), 98.6% (71 of 72), and 69.4% (25 of 36) for the 5-, 9-, and 17-stage ring oscillators, respectively. Because the yields of the 117 TEGs and 72 inverters were 100%, the reduced yield of the ring oscillators could be attributed to the noise margin of the inverters.

The fabricated devices are suitable for application as imperceptible wearable sensors because of their high mechanical flexibility. To assess the mechanical flexibility of the n-type transistors, bending tests were performed. The mechanical flexibility of the p-type transistors was assessed in our previous study.[33] We compared the transistor characteristics derived with and without bending. For comparison, the characteristics were first measured by placing the transistors on a flat surface (R = infinity), then again measured after rolling them along a cylinder with a radius of 0.6 mm (R = 0.6 mm), and finally, after crumpling (R = crumpling), as shown in Figure 7a,b. Figure 7c shows the transfer characteristics of the UV-illuminated and non-UV-illuminated n-type transistors obtained from each bending test. The transistor characteristics,

https://doi.org/10.1021/acsaelm.2c01444
ACS Appl. Electron. Mater. 2022, 4, 6308−6321

i.e., V_{on} and I_{DS}, did not change significantly after the transistors were rolled up as well as after they were crumpled. Figure 7d,e shows the V_{on} and I_{DS} plots at each bending condition, indicating that V_{on} and I_{DS} were almost identical in each test. The V_{on} of the transistors with and without UV illumination changed to 5 and 45 mV, respectively, after the test under the condition R = 0.6 mm and to 4 and 27 mV, respectively, after the test under the condition R = crumpling. The I_{DS} of the transistors with and without UV illumination changed by 1 and 7%, respectively, under the condition R = 0.6 mm and by 4 and 10%, respectively, under the condition R = crumpling. Furthermore, we performed cyclic bending tests to investigate the bending durability. The device was attached to a bending machine, in which the bending radius was set to 1 mm, as shown in Figure S19a,b. The transfer curves of the OTFTs were measured in intervals of 200 bending cycles up to 1000 cycles. Figure S19c,d shows the V_{on} and $|I_{DS}|$ plots normalized by the results when the bending cycle was 0. Negligible changes in V_{on} and $|I_{DS}|$ were observed after the 1000 bending cycles. Thus, these results, together with the previously demonstrated high mechanical flexibility of p-type transistors (demonstrated in our previous study), validate the ultraflexibility of the fabricated organic complementary circuits.

Finally, we demonstrated that the nanoscale interfacial photochemical reaction for the OTFTs can facilitate biosignal measurements. In this study, we measured EMG signals, which have a high-frequency component among biological signals, and demonstrated that the "depletion-mode" inverter (high-speed inverter) can measure the EMG signals more accurately than the "enhancement-mode" inverter (low-power inverter). As shown in Figure 8a, two electrodes were attached to the arms to extract the EMG signals. The compound action potentials were generated by squeezing the muscles in the arms. The input EMG signals (V_{in}) were passed through a complementary organic inverter and then extracted as output (V_{out}) through a buffer circuit and a two-channel analogue-to-digital converter (PowerLab, AD instrument, Dunedin, New Zealand). The reference EMG signals (V_{ref}) were monitored via another wire without passing them through the inverter. A "depletion-like mode" inverter was used as an amplifier, which is suitable for measuring high-frequency signals, including the EMG signals. The two supply voltages (V_{dd} and V_{ss}) were input while satisfying the relation $V_{dd} - V_{ss} = 4$ V such that the voltage of the input EMG signals would meet the trip point of the inverter. Figure 8b compares the power spectra of V_{ref} and V_{out}. The frequency components of the measured signals are broad in the near DC to 100 Hz range, suggesting that these are surface EMG signals; the power amplification gain is ∼100. For comparison, Figure S20a shows the power spectra of V_{ref} and V_{out} obtained using an "enhancement-like mode" inverter. Figure 8c shows the EMG waveforms as V_{ref} and V_{out}. A clear difference is observed between the resting potentials and the compound action potentials. The expanded compound action potentials between 0 and 0.5 s are displayed and compared as V_{ref} and V_{out}, indicating that the waveforms are well consistent. The coefficient of correlation between V_{ref} and V_{out} is −0.73. Figure S20b shows the V_{ref} and V_{out} waveforms obtained when the enhancement-like mode inverter was used. Although amplification is evident in some peaks, the correlation coefficient is −0.43. This result indicates that for EMG measurements, signal amplification can be obtained only using a "depletion-like mode" inverter. Notably, the power consumption is estimated to be 640 nW for the "depletion-like mode" inverter and 380 nW for the "enhancement-like mode" inverter; the "enhancement-like mode" inverter shows lower power consumption. Therefore, it is preferable to use the "enhancement-like mode" inverter for measuring biosignals with low-frequency components, such as chemical signals. These results collectively indicate that nanoscale interfacial photochemical reactions for OTFTs can be used for tuning the circuit performances according to the target biosignals.

CONCLUSIONS

In this study, the power consumption and operating speed of ultraflexible organic circuits integrated on a single substrate were finely tuned through a nanoscale interfacial photochemical reaction with a photoreactive gate dielectric, PNDPE. Organic complementary inverters and ring oscillators were fabricated on a large area (6 cm × 10 cm) and an ultraflexible (total thickness < 2.4 μm) single substrate. The V_{on} of the n-type OTFTs was controlled from −1.2 to −0.4 V with a standard deviation of 32 to 87 mV by changing the UV dose. TOF-SIMS analysis of the fabricated circuits implied that the V_{on} of the OTFTs, fabricated on a single substrate, is controlled one-by-one by patterning the UV-illuminated area and that the V_{on} shift is correlated to the interfacial photochemical reaction. The power consumption and operating speed of the inverters were tuned by a factor of approximately 6 and 4, respectively, on a single substrate. A minimum power consumption of 30 ± 9 pW at its transient and 4 ± 1 pW at standby was observed using the "enhancement-like mode" inverters, indicating that among the known OTFTs containing polymer gate dielectrics, our "enhancement-like mode" devices consume the lowest amount of power. Within the tuning range of the inverter operating speed, the "depletion-like mode" inverters exhibited a minimum stage delay time of the order of hundreds of microseconds at a supply voltage of 2.5 V. The fabricated inverters were operated at 0.2 V, and thus a large number of energy sources can be used to drive these devices, including biofuel cells. The fabricated devices show high mechanical flexibility. Furthermore, we demonstrated EMG measurements with PNDPE, suggesting that the nanoscale interfacial photochemical reaction for OTFTs can be used for tuning the circuit performances according to the target biosignals. The demonstrated nanoscale interfacial photochemical reaction with PNDPE is expected to propel the development of imperceptible wearable multimodal sensors containing organic signal processing circuits for long-term monitoring with low power consumption.

METHODS

Materials. Parylene (diX-SR) was provided by Daisan Kasei (Tokyo, Japan). DNTT was purchased from Nippon Chemical Industrial Co., Ltd (Tokyo, Japan), TU-1 was purchased from Tokyo Chemical Industry Co., Ltd. (Tokyo, Japan), and Cytop was purchased from AGC Inc. (Tokyo, Japan). PNDPE was synthesized according to a previously reported procedure.[35] In this case, powdered PNDPE was dissolved in anisole at a concentration of 10 mg mL^{-1} and sonicated for several hours. The solution was then stored in the dark for a few days and subsequently filtered by a mesh with a 45-μm pore radius.

Device Fabrication. The devices were fabricated using a previously reported process, as described here.[33] First, a thin layer of Cytop was spin-coated on a fluorinated glass substrate, followed by the formation of an ultraflexible 1-μm-thick parylene film by chemical vapor deposition (SCS Labcoter, Specialty Coating Systems Inc.,

https://doi.org/10.1021/acsaelm.2c01444
ACS Appl. Electron. Mater. 2022, 4, 6308−6321

Indiana). Next, a 100-nm-thick aluminum gate electrode was thermally evaporated, through a shadow mask, using a vacuum evaporator (EX-200, ULVAC, Inc., Kanagawa, Japan). The aluminum gate electrode was anodized using citric acid (500 mL, 1 mmol) as the electrolyte and a Pt electrode as the cathode to form an alumina (AlO_x) layer, which was then treated with oxygen plasma at 100 W for 30 s to reduce the impurities on it. The PNDPE was then spun at 500 rpm for 5 s and at 3000 rpm for the next 20 s. The PNDPE films were baked at 60 °C for 1.5 h to reduce the residual solvent. A handy-type Hg lamp (λ_p = 254 nm, P = 0.2 mW cm^{-2} at the sample surface) (SUV-16, AS ONE CORPORATION, Osaka, Japan) was used to illuminate the films through shadow masks to induce the photo-Fries rearrangement. Then, 20-nm-thick DNTT and TU-1 layers were thermally evaporated at an evaporation rate of 0.03 and 0.01 nm s^{-1}, respectively. Next, the source and drain electrodes were formed by thermally evaporating gold at a substrate temperature of −10 °C to suppress the thermal expansion of the shadow masks. The device was passivated by a 1-μm-thick parylene film to place the device at a neutral strain position. Finally, the source and drain electrodes were extracted out through holes formed by a 532 nm laser (T-Centric MD-T1000W, KEYENCE CORPORATION, Osaka, Japan) and the gold layer on the top of the device.

Measurements and Analyses. To measure the thickness of the PNDPE film formed on the silicon surface, it was first scratched by a brass tweezer and then scanned by a stylus surface profiler (DektakXT, Bruker Corp., Massachusetts). The transfer and output curves of the transistors were measured by a semiconductor parameter analyzer (B1500A, Keysight Technologies, Inc., California). V_{on} was defined as the cross-section point between the subthreshold slope and the 10^{-12} A current line. The mass spectra and depth profile images were acquired by TOF-SIMS (TOF.SIMS5, ION-TOF GmbH, Muenster, Germany), in which Bi_3^{++} ions were used as the primary ions. The acceleration and post-acceleration voltages of the Bi_3^{++} ions were 25 and 9.5 kV, respectively. The pulse width of the launched Bi_3^{++} ions was 17.8 ns, which was compressed by bunching. The positive and negative secondary ions were scanned in an area of 300 μm^2. In total, 16 scans were performed with 256 pixels per scan. The vacuum pressure was less than 4 × 10^{-7} Pa. The PNDPE film was formed on a highly doped silicon and silica substrate to suppress the charging. To evaluate the operation speed of the ring oscillator precisely, a commercially available voltage buffer was installed at the last stage of the ring oscillator. To obtain the depth profile and cross-sectional images, the PNDPE films were etched by Ar-ion clusters. A cyclic bending test was performed with a bending machine (Tension-Free Folding Clamshell-type Jig DMX-CS, Yuasa System Co., Ltd., Okayama, Japan). The transistors were set to the folded position of the machine such that the bending radius was 1 mm. In the EMG measurements, the offset voltages of V_{ref} and V_{out} were suppressed by differentiating the results with the moving average. V_{ref} and V_{out} were filtered through a mains filter.

■ ASSOCIATED CONTENT

Supporting Information

The Supporting Information is available free of charge at https://pubs.acs.org/doi/10.1021/acsaelm.2c01444.

Detailed fabrication processes and device characteristics of OTFTs and organic circuits; TOF-SIMS analysis of the PNDPE film; and comparison between the performance of the devices fabricated in this study and in other studies (PDF)

■ AUTHOR INFORMATION

Corresponding Authors

Takafumi Uemura − *SANKEN (The Institute of Scientific and Industrial Research), Osaka University, Ibaraki, Osaka 567-0047, Japan; Advanced Photonics and Biosensing Open Innovation Laboratory, National Institute of Advanced Industrial Science and Technology (AIST), Suita, Osaka 565-0871, Japan;* orcid.org/0000-0002-0051-2909; Phone: +81-6-6879-8402; Email: uemura-t@sanken.osaka-u.ac.jp

Tsuyoshi Sekitani − *SANKEN (The Institute of Scientific and Industrial Research), Osaka University, Ibaraki, Osaka 567-0047, Japan; Graduate School of Engineering, Osaka University, Suita, Osaka 565-0871, Japan; Advanced Photonics and Biosensing Open Innovation Laboratory, National Institute of Advanced Industrial Science and Technology (AIST), Suita, Osaka 565-0871, Japan;* orcid.org/0000-0003-1070-2738; Phone: +81-6-6879-8400; Email: sekitani.tsuyoshi.sanken@osaka-u.ac.jp

Authors

Koki Taguchi − *SANKEN (The Institute of Scientific and Industrial Research), Osaka University, Ibaraki, Osaka 567-0047, Japan; Graduate School of Engineering, Osaka University, Suita, Osaka 565-0871, Japan; Advanced Photonics and Biosensing Open Innovation Laboratory, National Institute of Advanced Industrial Science and Technology (AIST), Suita, Osaka 565-0871, Japan;* orcid.org/0000-0003-3358-2230

Andreas Petritz − *JOANNEUM RESEARCH Forschungsgesellschaft mbH MATERIALS-Institute for Surface Technologies and Photonics, Weiz 8160, Austria;* orcid.org/0000-0001-8158-0112

Naoko Namba − *SANKEN (The Institute of Scientific and Industrial Research), Osaka University, Ibaraki, Osaka 567-0047, Japan; Advanced Photonics and Biosensing Open Innovation Laboratory, National Institute of Advanced Industrial Science and Technology (AIST), Suita, Osaka 565-0871, Japan*

Mihoko Akiyama − *SANKEN (The Institute of Scientific and Industrial Research), Osaka University, Ibaraki, Osaka 567-0047, Japan; Graduate School of Engineering, Osaka University, Suita, Osaka 565-0871, Japan;* orcid.org/0000-0003-1690-3581

Masahiro Sugiyama − *SANKEN (The Institute of Scientific and Industrial Research), Osaka University, Ibaraki, Osaka 567-0047, Japan; Graduate School of Engineering, Osaka University, Suita, Osaka 565-0871, Japan; Advanced Photonics and Biosensing Open Innovation Laboratory, National Institute of Advanced Industrial Science and Technology (AIST), Suita, Osaka 565-0871, Japan*

Teppei Araki − *SANKEN (The Institute of Scientific and Industrial Research), Osaka University, Ibaraki, Osaka 567-0047, Japan; Graduate School of Engineering, Osaka University, Suita, Osaka 565-0871, Japan; Advanced Photonics and Biosensing Open Innovation Laboratory, National Institute of Advanced Industrial Science and Technology (AIST), Suita, Osaka 565-0871, Japan*

Barbara Stadlober − *JOANNEUM RESEARCH Forschungsgesellschaft mbH MATERIALS-Institute for Surface Technologies and Photonics, Weiz 8160, Austria;* orcid.org/0000-0002-4572-7129

Complete contact information is available at: https://pubs.acs.org/10.1021/acsaelm.2c01444

Author Contributions

K.T. performed the experiments and analyzed the results. K.T., T.U., and T.S. conceived and designed this project. T.U. and T.S. supervised this research. K.T. wrote the manuscript. All

https://doi.org/10.1021/acsaelm.2c01444
ACS Appl. Electron. Mater. 2022, 4, 6308−6321

the authors contributed to the discussion and finalization of the manuscript.

Notes

The authors declare no competing financial interest.

■ ACKNOWLEDGMENTS

This study was supported by the Japan Society for the Promotion of Science (JSPS) KAKENHI (grant numbers 22H00588, 22H01940, 22K18975, 22J14062, and 22H01553); JSPS Bilateral Program Number JPJSBP120222002; JST FOREST Program (grant numbers JPMJFR2035 and JPMJFR2022, Japan); JST COI-NEXT (Grant Number JPMJPF2115); JST Moonshot R&D Program (Grant Number JPMJMS2012); JPNP20004 subsidized by the New Energy and Industrial Technology Development Organization (NEDO); Crossover Alliance to Create the Future with People, Intelligence and Materials; Advanced Research Infrastructure for Materials and Nanotechnology (ARIM) (Grant No. JPMXP1222OS1002); Advanced Photonics and Biosensing Open Innovation Laboratory, the National Institute of Advanced Industrial Science and Technology (AIST); Tateisi Science and Technology Foundation; and FWF Austrian Science Fund (Vienna, AT) (J4145-N30). The authors would like to thank Krzysztof Krawczyk (JOANNEUM RESEARCH Forschungsgesellschaft mbH, Austria) for the synthesis of the PNDPE material, Esther Karner-Petritz (JOANNEUM RESEARCH Forschungsgesellschaft mbH, Austria) for preparing the PNDPE solution, Daisan Kasei for providing diX-SR, and Editage (www.editage.com) for English language editing.

■ REFERENCES

(1) Myny, K. The Development of Flexible Integrated Circuits Based on Thin-Film Transistors. *Nat. Electron.* **2018**, *1*, 30−39.
(2) Liu, Y.; Pharr, M.; Salvatore, G. A. Lab-on-Skin: A Review of Flexible and Stretchable Electronics for Wearable Health Monitoring. *ACS Nano* **2017**, *11*, 9614−9635.
(3) Kim, J.; Campbell, A. S.; de Ávila, B. E. F.; Wang, J. Wearable Biosensors for Healthcare Monitoring. *Nat. Biotechnol.* **2019**, *37*, 389−406.
(4) Fang, H.; Yu, K. J.; Gloschat, C.; Yang, Z.; Song, E.; Chiang, C. H.; Zhao, J.; Won, S. M.; Xu, S.; Trumpis, M.; Zhong, Y.; Han, S. W.; Xue, Y.; Xu, D.; Choi, S. W.; Cauwenberghs, G.; Kay, M.; Huang, Y.; Viventi, J.; Efimov, I. R.; Rogers, J. A. Capacitively Coupled Arrays of Multiplexed Flexible Silicon Transistors for Long-Term Cardiac Electrophysiology. *Nat. Biomed. Eng.* **2017**, *1*, No. 0038.
(5) Reeder, J.; Kaltenbrunner, M.; Ware, T.; Arreaga-Salas, D.; Avendano-Bolivar, A.; Yokota, T.; Inoue, Y.; Sekino, M.; Voit, W.; Sekitani, T.; Someya, T. Mechanically Adaptive Organic Transistors for Implantable Electronics. *Adv. Mater.* **2014**, *26*, 4967−4973.
(6) Sekitani, T.; Yokota, T.; Kuribara, K.; Kaltenbrunner, M.; Fukushima, T.; Inoue, Y.; Sekino, M.; Isoyama, T.; Abe, Y.; Onodera, H.; Someya, T. Ultraflexible Organic Amplifier with Biocompatible Gel Electrodes. *Nat. Commun.* **2016**, *7*, No. 11425.
(7) Salvatore, G. A.; Münzenrieder, N.; Kinkeldei, T.; Petti, L.; Zysset, C.; Strebel, I.; Büthe, L.; Tröster, G. Wafer-Scale Design of Lightweight and Transparent Electronics That Wraps around Hairs. *Nat. Commun.* **2014**, *5*, No. 2982.
(8) Xiang, L.; Zeng, X.; Xia, F.; Jin, W.; Liu, Y.; Hu, Y. Recent Advances in Flexible and Stretchable Sensing Systems: From the Perspective of System Integration. *ACS Nano* **2020**, *14*, 6449−6469.
(9) Zeng, X.; Hu, Y. Sensation and Perception of a Bioinspired Flexible Smart Sensor System. *ACS Nano* **2021**, *15*, 9238−9243.
(10) Gao, W.; Emaminejad, S.; Nyein, H. Y. Y.; Challa, S.; Chen, K.; Peck, A.; Fahad, H. M.; Ota, H.; Shiraki, H.; Kiriya, D.; Lien, D. H.; Brooks, G. A.; Davis, R. W.; Javey, A. Fully Integrated Wearable Sensor Arrays for Multiplexed in Situ Perspiration Analysis. *Nature* **2016**, *529*, 509−514.
(11) Lu, Y.; Xu, K.; Zhang, L.; Deguchi, M.; Shishido, H.; Arie, T.; Pan, R.; Hayashi, A.; Shen, L.; Akita, S.; Takei, K. Multimodal Plant Healthcare Flexible Sensor System. *ACS Nano* **2020**, *14*, 10966−10975.
(12) Hozumi, S.; Honda, S.; Arie, T.; Akita, S.; Takei, K. Multimodal Wearable Sensor Sheet for Health-Related Chemical and Physical Monitoring. *ACS Sens.* **2021**, *6*, 1918−1924.
(13) Xu, Y.; Guo, W.; Zhou, S.; Yi, H.; Yang, G.; Mei, S.; Zhu, K.; Wu, H.; Li, Z. Bioinspired Perspiration-Wicking Electronic Skins for Comfortable and Reliable Multimodal Health Monitoring. *Adv. Funct. Mater.* **2022**, *32*, No. 2200961.
(14) Liu, H.; Xiang, H.; Wang, Y.; Li, Z.; Qian, L.; Li, P.; Ma, Y.; Zhou, H.; Huang, W. A Flexible Multimodal Sensor That Detects Strain, Humidity, Temperature, and Pressure with Carbon Black and Reduced Graphene Oxide Hierarchical Composite on Paper. *ACS Appl. Mater. Interfaces* **2019**, *11*, 40613−40619.
(15) Wang, B.; Thukral, A.; Xie, Z.; Liu, L.; Zhang, X.; Huang, W.; Yu, X.; Yu, C.; Marks, T. J.; Facchetti, A. Flexible and Stretchable Metal Oxide Nanofiber Networks for Multimodal and Monolithically Integrated Wearable Electronics. *Nat. Commun.* **2020**, *11*, No. 2405.
(16) Fuketa, H.; Yoshioka, K.; Shinozuka, Y.; Ishida, K. Measurement Sheet With 2 V Organic Transistors for Prosthetic Hand Control. *IEEE Trans. Biomed. Eng.* **2014**, *8*, 824−833.
(17) Sekitani, T.; Zschieschang, U.; Klauk, H.; Someya, T. Flexible Organic Transistors and Circuits with Extreme Bending Stability. *Nat. Mater.* **2010**, *9*, 1015−1022.
(18) Fukuda, K.; Someya, T. Recent Progress in the Development of Printed Thin-Film Transistors and Circuits with High-Resolution Printing Technology. *Adv. Mater.* **2017**, *29*, No. 1602736.
(19) Matsui, H.; Takeda, Y.; Tokito, S. Flexible and Printed Organic Transistors: From Materials to Integrated Circuits. *Org. Electron.* **2019**, *75*, No. 105432.
(20) Zschieschang, U.; Ante, F.; Schlörholz, M.; Schmidt, M.; Kern, K.; Klauk, H. Mixed Self-Assembled Monolayer Gate Dielectrics for Continuous Threshold Voltage Control in Organic Transistors and Circuits. *Adv. Mater.* **2010**, *22*, 4489−4493.
(21) Zschieschang, U.; Bader, V. P.; Klauk, H. Below-One-Volt Organic Thin-Film Transistors with Large on/off Current Ratios. *Org. Electron.* **2017**, *49*, 179−186.
(22) Baeg, K. J.; Khim, D.; Kim, J.; Han, H.; Jung, S. W.; Kim, T. W.; Kang, M.; Facchetti, A.; Hong, S. K.; Kim, D. Y.; Noh, Y. Y. Controlled Charge Transport by Polymer Blend Dielectrics in Top-Gate Organic Field-Effect Transistors for Low-Voltage-Operating Complementary Circuits. *ACS Appl. Mater. Interfaces* **2012**, *4*, 6176−6184.
(23) Dao, T. T.; Sakai, H.; Nguyen, H. T.; Ohkubo, K.; Fukuzumi, S.; Murata, H. Controllable Threshold Voltage in Organic Complementary Logic Circuits with an Electron-Trapping Polymer and Photoactive Gate Dielectric Layer. *ACS Appl. Mater. Interfaces* **2016**, *8*, 18249−18255.
(24) Nastasi, M.; Mayer, J. W. *Ion Implantation and Synthesis of Materials*; Springer, 2006; p 111.
(25) Hirata, I.; Zschieschang, U.; Yokota, T.; Kuribara, K.; Kaltenbrunner, M.; Klauk, H.; Sekitani, T.; Someya, T. High-Resolution Spatial Control of the Threshold Voltage of Organic Transistors by Microcontact Printing of Alkyl and Fluoroalkylphosphonic Acid Self-Assembled Monolayers. *Org. Electron.* **2015**, *26*, 239−244.
(26) Fukuda, K.; Sekitani, T.; Zschieschang, U.; Klauk, H.; Kuribara, K.; Yokota, T.; Sugino, T.; Asaka, K.; Ikeda, M.; Kuwabara, H.; Yamamoto, T.; Takimiya, K.; Fukushima, T.; Aida, T.; Takamiya, M.; Sakurai, T.; Someya, T. A 4 V Operation, Flexible Braille Display Using Organic Transistors, Carbon Nanotube Actuators, and Organic Static Random-Access Memory. *Adv. Funct. Mater.* **2011**, *21*, 4019−4027.
(27) Lashkov, I.; Krechan, K.; Ortstein, K.; Talnack, F.; Wang, S. J.; Mannsfeld, S. C. B.; Kleemann, H.; Leo, K. Modulation Doping for

https://doi.org/10.1021/acsaelm.2c01444
ACS Appl. Electron. Mater. 2022, 4, 6308−6321

Threshold Voltage Control in Organic Field-Effect Transistors. *ACS Appl. Mater. Interfaces* **2021**, *13*, 8664−8671.
(28) Lee, B. H.; Bazan, G. C.; Heeger, A. J. Doping-Induced Carrier Density Modulation in Polymer Field-Effect Transistors. *Adv. Mater.* **2016**, *28*, 57−62.
(29) Marchl, M.; Edler, M.; Haase, A.; Fian, A.; Trimmel, G.; Griesser, T.; Stadlober, B.; Zojer, E. Tuning the Threshold Voltage in Organic Thin-Film Transistors by Local Channel Doping Using Photoreactive Interfacial Layers. *Adv. Mater.* **2010**, *22*, 5361−5365.
(30) Petritz, A.; Wolfberger, A.; Fian, A.; Krenn, J. R.; Griesser, T.; Stadlober, B. High Performance P-Type Organic Thin Film Transistors with an Intrinsically Photopatternable, Ultrathin Polymer Dielectric Layer. *Org. Electron.* **2013**, *14*, 3070−3082.
(31) Montaigne Ramil, A.; Hernandez-Sosa, G.; Griesser, T.; Simbrunner, C.; Höfler, T.; Trimmel, G.; Kern, W.; Shen, Q.; Teichert, C.; Schwabegger, G.; Sitter, H.; Sariciftci, N. S. Photo-Fries-Based Photosensitive Polymeric Interlayers for Patterned Organic Devices. *Appl. Phys. A: Mater. Sci. Process.* **2012**, *107*, 985−993.
(32) Gold, H.; Petritz, A.; Karner-Petritz, E.; Tschepp, A.; Groten, J.; Prietl, C.; Scheipl, G.; Zirkl, M.; Stadlober, B. Flexible Single-Substrate Integrated Active-Matrix Pyroelectric Sensor. *Phys. Status Solidi RRL* **2019**, *13*, No. 1900277.
(33) Taguchi, K.; Uemura, T.; Namba, N.; Petritz, A.; Araki, T.; Sugiyama, M.; Stadlober, B.; Sekitani, T. Heterogeneous Functional Dielectric Patterns for Charge-Carrier Modulation in Ultraflexible Organic Integrated Circuits. *Adv. Mater.* **2021**, *33*, No. 2104446.
(34) Torres-Miranda, M.; Petritz, A.; Karner-Petritz, E.; Prietl, C.; Sauter, E.; Zharnikov, M.; Gold, H.; Stadlober, B. Characterization and Compact Modeling of Self-Aligned Short-Channel Organic Transistors. *IEEE Trans. Electron Devices* **2018**, *65*, 4563−4570.
(35) Höfler, T.; Grießer, T.; Gstrein, X.; Trimmel, G.; Jakopic, G.; Kern, W. UV Reactive Polymers for Refractive Index Modulation Based on the Photo-Fries Rearrangement. *Polymer* **2007**, *48*, 1930−1939.
(36) Schmidt, E. M.; Mcintosh, J. S.; Bak, M. J. Long-Term Implants of Parylene-C Coated Microelectrodes. *Med. Biol. Eng. Comput.* **1988**, *26*, 96−101.
(37) Rodger, D. C.; Weiland, J. D.; Humayun, M. S.; Tai, Y. C. Scalable High Lead-Count Parylene Package for Retinal Prostheses. *Sens. Actuators, B* **2006**, *117*, 107−114.
(38) Mamada, M.; Shima, H.; Yoneda, Y.; Shimano, T.; Yamada, N.; Kakita, K.; Machida, T.; Tanaka, Y.; Aotsuka, S.; Kumaki, D.; Tokito, S. A Unique Solution-Processable n-Type Semiconductor Material Design for High-Performance Organic Field-Effect Transistors. *Chem. Mater.* **2015**, *27*, 141−147.
(39) Baeg, K. J.; Khim, D.; Jung, S. W.; Kang, M.; You, I. K.; Kim, D. Y.; Facchetti, A.; Noh, Y. Y. Remarkable Enhancement of Hole Transport in Top-Gated N-Type Polymer Field- Effect Transistors by a High-K Dielectric for Ambipolar Electronic Circuits. *Adv. Mater.* **2012**, *24*, 5433−5439.
(40) SDBSWeb: https://sdbs.db.aist.go.jp (National Institute of Advanced Industrial Scienceand Technology, 2022).
(41) Shiwaku, R.; Matsui, H.; Hayasaka, K.; Takeda, Y.; Fukuda, T.; Kumaki, D.; Tokito, S. Printed Organic Inverter Circuits with Ultralow Operating Voltages. *Adv. Electron. Mater.* **2017**, *3*, No. 1600557.
(42) Kwon, C. H.; Lee, S. H.; Choi, Y. B.; Lee, J. A.; Kim, S. H.; Kim, H. H.; Spinks, G. M.; Wallace, G. G.; Lima, M. D.; Kozlov, M. E.; Baughman, R. H.; Kim, S. J. High-Power Biofuel Cell Textiles from Woven Biscrolled Carbon Nanotube Yarns. *Nat. Commun.* **2014**, *5*, No. 3928.

https://doi.org/10.1021/acsaelm.2c01444
ACS Appl. Electron. Mater. 2022, 4, 6308−6321